BIOCHEMISTRY
including biophysical chemistry & molecular biology
Article

Biochemistry **2010,** *49,* 3989–4000 3989
DOI: 10.1021/bi1001954

The Structures of the C185S and C185A Mutants of Sulfite Oxidase Reveal Rearrangement of the Active Site†

James A. Qiu,‡,⊥ Heather L. Wilson,‡ M. Jake Pushie,§,⊥ Caroline Kisker,∥ Graham N. George,§ and K. V. Rajagopalan*,‡

‡*Department of Biochemistry, Duke University Medical Center, Durham, North Carolina 27710,* §*Department of Geological Sciences, University of Saskatchewan, Saskatoon, Saskatchewan S7N E52, Canada, and* ∥*Rudolf Virchow Center for Experimental Biomedicine, University of Würzburg, Josef-Schneider-Strasse 2, 97080 Würzburg, Germany.* ⊥*These authors contributed equally to this work.*

Received February 8, 2010; Revised Manuscript Received March 30, 2010

ABSTRACT: Sulfite oxidase (SO) catalyzes the physiologically critical conversion of sulfite to sulfate. Enzymatic activity is dependent on the presence of the metal molybdenum complexed with a pyranopterin-dithiolene cofactor termed molybdopterin. Comparison of the amino acid sequences of SOs from a variety of sources has identified a single conserved Cys residue essential for catalytic activity. The crystal structure of chicken liver sulfite oxidase indicated that this residue, Cys185 in chicken SO, coordinates the Mo atom in the active site. To improve our understanding of the role of this residue in the catalytic mechanism of sulfite oxidase, serine and alanine variants at position 185 of recombinant chicken SO were generated. Spectroscopic and kinetic studies indicate that neither variant is capable of sulfite oxidation. The crystal structure of the C185S variant was determined to 1.9 Å resolution and to 2.4 Å resolution in the presence of sulfite, and the C185A variant to 2.8 Å resolution. The structures of the C185S and C185A variants revealed that neither the Ser or Ala side chains appeared to closely interact with the Mo atom and that a third oxo group replaced the usual cysteine sulfur ligand at the Mo center, confirming earlier extended X-ray absorption fine structure spectroscopy (EXAFS) work on the human C207S mutant. An unexpected result was that in the C185S variant, in the absence of sulfite, the active site residue Tyr322 became disordered as did the loop region flanking it. In the C185S variant crystallized in the presence of sulfite, the Tyr322 residue relocalized to the active site. The C185A variant structure also indicated the presence of a third oxygen ligand; however, Tyr322 remained in the active site. EXAFS studies of the Mo coordination environment indicate the Mo atom is in the oxidized Mo^{VI} state in both the C185S and C185A variants of chicken SO and show the expected trioxo-dithiolene active site. Density functional theory calculations of the trioxo form of the cofactor reasonably reproducd the Mo=O distances of the complex; however, the calculated Mo−S distances were slightly longer than either crystallographic or EXAFS measurements. Taken together, these results indicate that the active sites of the C185S and C185A variants are essentially catalytically inactive, the crystal structures of C185S and C185A variants contain a fully oxidized, trioxo form of the cofactor, and Tyr322 can undergo a conformational change that is relevant to the reaction mechanism. Additional DFT calculations demonstrated that such methods can reasonably reproduce the geometry and bond lengths of the active site.

Sulfite oxidase (SO) from higher eukaryotes is an essential enzyme that requires the presence of the molybdenum cofactor (Moco) (*1*), a prosthetic group complex comprised of the transition element Mo with an organic pyranopterin-dithiolene moiety termed molybdopterin (MPT) that coordinates the Mo center via the two sulfurs of the dithiolene group (*2*). Vertebrate SO also contains a second prosthetic group, a porphyrin iron heme group. SO catalyzes the oxidation of sulfite to sulfate in the metabolism of sulfur-containing compounds such as the amino acids Met and Cys. SO catalyzes this reaction via the two-electron oxidation of sulfite to sulfate, using cytochrome *c* (cyt *c*) as the physiological electron acceptor, as seen in reaction 1.

$$SO_3^{2-} + H_2O + 2(\text{cyt } c)_{ox} \rightarrow SO_4^{2-} + 2(\text{cyt } c)_{red} + 2H^+ \quad (1)$$

In the reductive half-reaction, sulfite binds to the Mo^{VI} center and is oxidized to sulfate, with concomitant reduction of the Mo center by two electrons to yield a $Mo^{IV}Fe^{III}$ species. In the first intramolecular electron transfer (IET), one of the electrons is transferred from the Mo^{IV} to the N-terminal heme group to yield the Mo^{V} Fe^{II} species that can be observed by electron paramagnetic resonance (EPR) (*3*). In the oxidative half-reaction, one electron is transferred from the Fe^{II} to cyt c_{ox} to yield Fe^{III}. This is followed by a second IET step in which Mo^{V} donates another electron to Fe^{III}. The enzyme becomes fully oxidized when the Fe^{II} reduces a second molecule of cyt *c* to yield the Mo^{VI} Fe^{III} form of SO. The distance between the Mo and heme Fe atoms in the structure of chicken SO (CSO) purified from hepatic tissue is approximately 32 Å. This distance is greater than what would be

†Work at Duke University was supported by National Institutes of Health (NIH) Grant GM00091 to K.V.R. Work at the University of Saskatchewan was supported by a Natural Sciences and Engineering Research Council (Canada) (G.N.G.), with further support from the Saskatchewan Health Research Foundation, a Canada Research Chair award (to G.N.G.), and the Canadian Institutes for Health Research. Work at the University of Würzburg was supported by the Deutsche Forschungsgemeinschaft (DFG) (Forschungszentrum FZ82) to C.K.

*To whom correspondence should be addressed: Department of Biochemistry, Box 3711, Duke University Medical Center, Durham, NC 27710. Telephone: (919) 681-8845. Fax: (919) 684-8885. E-mail: raj@biochem.duke.edu.

Published on Web 03/31/2010

expected for the observed rate of electron transfer (*4*). One explanation for this discrepancy is that high-efficiency electron transfer could occur via the main chain atoms through the active site residue Arg138 (*4*). Alternatively, a conformational change that would bring the heme group closer to the Moco could also explain the high rate of IET. Studies on the rate of SO IET show a correlation between IET and the viscosity of the solution, supporting the importance of a conformational change (*5*).

SO deficiency in humans is a rare and devastating inborn error of metabolism. This deficiency arises either from mutations in the biosynthetic pathway of Moco, leading to combined MPT deficiency (*6*), or from point mutations in the gene encoding SO itself that result in isolated SO deficiency (*7*). Symptoms of SO deficiency include severe neurological effects such as seizures, mental retardation, attenuated brain development, and detached retinas, and SO deficiency generally results in death at an early age (*8*, *9*). It has been suggested that the pathology associated with SO deficiency is due to a toxic buildup of sulfite in the developing brain (*10*). Excess sulfite can react with disulfide bonds to form sulfonated Cys residues that have been shown to disrupt the disulfide bonds critical for protein tertiary structure (*11*). In addition, a lack of sulfate in the brain may interfere with the production of sulfatides, lipid sulfate esters found in the white matter of the brain and a component of myelin (*8*, *12*). The complete amino acid sequences of SO from human (*13*), rat (*14*), and chicken (*15*, *16*) sources have been reported previously.

Structure−function studies of human SO (HSO) would be advantageous in elucidating the mechanism of SO deficiency. Unfortunately, HSO has so far proven to be intractable for crystallization. The homologous chicken sulfite oxidase (CSO) protein shares 68% sequence identity with HSO. CSO has been purified from the source and characterized and the crystal structure determined to 1.9 Å resolution (*4*). CSO exists as a homodimer in the mitochondrial intermembrane space. The monomer of the enzyme can be divided into three domains. The N-terminal domain, up to residue 84, contains Fe bound in a heme group and is similar to bovine cytochrome b_5 by structural alignment. The central domain contains the Moco and the active site and is composed of residues 96−323. The C-terminal domain is the site of formation of the dimer between SO monomers and is similar to members of the C2 class of immunoglobulins (*4*). The N-terminal heme domain is connected to the central domain via a flexible linker region that was poorly defined in the electron density of the original structure of chicken sulfite oxidase (*4*). The active site of the enzyme contains three positively charged residues (Arg138, Arg190, and Arg450) and two polar residues (Tyr322 and Trp204) that surround the active site. The CSO structure revealed that the Mo atom is coordinated to two oxo groups, two MPT dithiolene sulfurs, and the thiolate group from Cys185 in a square pyramidal coordination geometry. Unfortunately, mutational analysis of native CSO was not possible as multiple attempts to clone the gene have proven to be difficult, and sequencing of the chicken genome has not identified the SO gene to date (*17*). Because of these factors, a major advance in the field was the creation of a synthetic gene for CSO (*16*), facilitating the expression of fully functional recombinant chicken SO (rCSO) expressed in *Escherichia coli* and the creation of rCSO variants for structure−function studies.

Sequence alignment of SO from various sources with the related molybdopterin enzyme nitrate reductase (NR) from fungal and plant sources has been reported, and it was shown that the two protein's heme domains are homologous and the Moco binding pockets are highly conserved (*18*−*21*). NR catalyzes the reduction of nitrate to nitrite, which is a vital step in nitrate assimilation in plants and fungi. The domains of NR are arranged in a manner opposite to that in SO, with an N-terminal Moco-containing domain, a central heme domain, and a C-terminal FAD binding domain. While the catalytic activities of NR and SO are in reverse directions (NR reduces its substrate while SO oxidizes its substrate), the two enzymes display a high degree of sequence homology. The *Arabidopsis thaliana* NR and *Gallus gallus* SO are 38% homologous in the Moco domain. Sequence alignments have identified a single conserved Cys residue in SO and NR enzymes from various sources (*22*). The importance of this Cys residue is further demonstrated by studies on the HSO variant C207S that displays severely decreased catalytic activity (Cys207 corresponds to Cys185 in CSO) (*23*). Extended X-ray absorption fine structure spectroscopy (EXAFS) studies on human C207S SO indicated that one of the three Mo−S bonds was lost, but a third oxo ligand was present, resulting in a fully oxidized trioxo form of the enzyme active site, in which Ser207 did not coordinate to the Mo center (*24*). A combination of redox potentiometry and EPR and EXAFS spectroscopies have extended this work, indicating that Ser207 does coordinate in the reduced Mo^{IV} form but dissociates upon reoxidation to Mo^{VI}, giving rise to the observed trioxo species (*23*).

On the basis of its proximity to the equatorial oxo ligand of Mo in the wild-type CSO crystal structure, Tyr322 has been implicated in preparing the reactive oxo group of Mo^{VI} for the transfer of oxygen to sulfite. CSO Tyr322 corresponds to HSO Tyr343, and the HSO Y343F variant has been generated. Kinetic studies have demonstrated a role for Tyr343 in catalysis, IET, and substrate binding (*25*, *26*).

In an effort to gain further insight into structural changes caused by active site mutations and to enhance our understanding of the role of the active site Cys residue in the mechanism of SO, the C185S and C185A variants of rCSO were generated, expressed, purified, and characterized. Spectroscopic and kinetic analysis of both the C185S and C185A variants determined that neither variant is capable of oxidizing sulfite to sulfate and both are catalytically inactive. The crystal structures of C185S in the absence and presence of its substrate sulfite, as well as the C185A variant, were determined. High-resolution crystal structures revealed a change in the coordination of the Mo center in all three structures, indicating that loss of the Cys sulfur bond results in a trioxo form of the active site, representing an unreactive oxidized form of the cofactor. Additionally, in the C185S structure, the active site Tyr322 and a loop region flanking it are disordered, while the presence of sulfite in the C185S variant as well as the C185A variant indicates that Tyr322 is present in a conformation similar to that of the wild-type enzyme rCSO. In an investigation of the Mo coordination environment of the C185S and C185A variants of rCSO, EXAFS confirmed that these variants are in the Mo^{VI} trioxo form, and density functional theory (DFT) structure calculations further supported the proposed structural model. Taken together, these results demonstrate the critical mechanistic role Cys185 plays in the active site of SO.

MATERIALS AND METHODS

Synthesis and Cloning of C185S and C185A rCSO Variants. The Transformer site-directed mutagenesis kit from Clonetech Laboratories Inc. was used to introduce the C185S mutation into pTRC CLSO.2, a plasmid expressing rCSO (*16*),

using the mutagenic primer GAC CTT GCA GTC CGC GGT AAC CGT and the selection primer CTG CGC TCG GCC CTT CCT GCA GGC TGG TTT which changes a BglI site to a PstI site as described previously (*25*). The C185A rCSO variant was created by overlapping primer extension PCR (*27*) using the flanking pTRC99a vector primers GAC ATC ATA ACG GTT CTG (coding) and TGT TTA TCA GAC CCG CTT C (anticoding) and the mutagenic primers GCG ACC CTG CAG GCG GCG GGT AAC CG (coding) and CGG TTA CCC GCC GCC TGC AGG GTC GC (anticoding) which convert the Cys185 position to Ala. All constructs were verified by sequencing at the Duke University DNA analysis facility, resulting in rCLSO_C185S and rCLSO_C185A expression plasmids.

Protein Expression and Purification. *E. coli* TP1000 cells (*mobA*-) (*28*) transformed with vector rCLSO_C185S were used for rCSO expression with a slightly modified protocol to maximize protein expression. The final 18 L cell culture was grown initially at 37 °C for 1 h, and then the temperature was reduced to 30 °C for an additional 14−16 h. The recombinant enzymes were purified through phenyl-Sepharose chromatography as described previously (*28*). As a final step, the enzyme was additionally purified using a Superdex-200 HR 16/60 size-exclusion column equilibrated with 50 mM potassium phosphate buffer attached to an AKTA FPLC system (Amersham/GE Healthcare) and eluted with a flow rate of 1 mL/min. The protein was stored in a buffer consisting of 50 mM potassium phosphate (pH 7.8) and 0.1 mM EDTA at 4 °C. The molybdenum content of the purified proteins was quantified by atomic absorption spectroscopy using a Varian Spectra AA-220 double-beam atomic absorption spectrometer. Samples were wet-ashed with nitric acid as described previously (*22*). UV−vis absorption spectra were recorded using 2.7 μM protein in a buffer containing 50 mM Tris (pH 7.5) adjusted using acetic acid to minimize small anion inhibition. The absorption spectra in the presence of sulfite were obtained using identical conditions with the addition of sodium sulfite to a final concentration of 1 mM (*16*, *23*, *29*) in a 1 cm path length quartz cuvette in a Shimadzu UV-1601 spectrophotometer.

Steady-State Kinetics. Steady-state kinetic assays were performed aerobically at 25 °C using a quartz cuvette with a 1 cm path length in a Shimadzu UV-1601 spectrophotometer. Assays were conducted in 50 mM buffers that were pH adjusted using acetic acid to minimize anion inhibition of SO (*30*). Bis-tris (pH 6.0), Bis-tris propane (pH 7.0), Tris (pH 8.0), and glycine (pH 9.0 and 10.0) were used as buffers. The glycine buffers were pH adjusted with NaOH. SO concentrations were determined from their A_{413} using a molar extinction coefficient of 113000 M^{-1} cm^{-1} per heme. The cyt *c* concentration was determined from the A_{550} using an extinction coefficient of 19630 M^{-1} cm^{-1}. Assay conditions were as follows: 50 mM cyt *c*, 2.5 μg SO, and varying concentrations of sodium sulfite in a final sample volume of 1 mL. SO activity was monitored by the reduction of cyt *c* at 550 nm. SO activity was also assayed in the C185S and C185A variants using ferricyanide, a small molecule nonspecific electron acceptor. Assay conditions were as follows: 40 mM ferricyanide, 5 μg of enzyme, and 50 mM buffers (observing the change in absorbance at 420 nm) in a final volume of 1 mL.

Crystallization and Data Collection. After purification, the buffer for the C185S variant was exchanged using a PD-10 ion exchange column into 20 mM Tris (pH 7.8) and 100 mM NaCl, and the protein was concentrated to 25 mg/mL using a Centricon YM-30 concentrator (GE Biosciences). This sample served as a stock protein solution and was stored at 4 °C prior to crystallization. From this stock solution, the protein was diluted to 10 mg/mL using a buffer containing 20 mM Tris (pH 7.8) and 100 mM NaCl. Crystals were obtained by the hanging drop vapor diffusion method at 17 °C, via addition of 2 μL of a protein solution to 2 μL of a precipitant solution equilibrated against 1 mL of reservoir crystallization solution containing 15% (v/v) MPD, 2% PEG 4000 (w/v), and 100 mM sodium acetate (pH 5.0). Red crystals were observed after 4 weeks and grew to their final size in 5−6 weeks. Crystals grew on a protein skin which had to be removed using microtools and then transferred to the crystallization solution containing 5% glycerol, the concentration of which was increased stepwise to a final concentration of 35%, as the cryoprotectant was then flash-frozen in liquid nitrogen. The crystals belong to space group $C222_1$ with a solvent content of 54.5% and the following unit cell dimensions: a = 86.46 Å, b = 131.51 Å, and c = 98.88 Å. The sulfite-bound crystal form was grown under slightly different crystallization conditions using 2% PEG 4000 (w/v), 10% MPD (v/v), 100 mM sodium acetate (pH 5.0), and 0.5 mM sodium sulfite by the hanging drop method as mentioned above. The crystals were observed after 3 weeks, reaching their final size by 6 weeks, and were again red in color. The crystals also grew in a precipitate skin on the hanging drop that required extraction. These crystals belonged to space group $I4_1$ with one molecule in the asymmetric unit and a solvent content of 54.9% with the following unit cell dimensions: a = 86.28 Å, b = 86.28 Å, and c = 152.33 Å. Crystals were cryocooled as described above. The C185A variant was crystallized in 15% (w/v) PEG 4000, 150 mM $(NH_4)_2SO_4$, and 100 mM MES (pH 6.0) using the sitting drop method; 300 nL of protein and 300 nL of precipitant solution were mixed against 100 μL of precipitant solution, and the crystals were grown at 17 °C. The crystal appeared after 2 days and grew to its final size in 6 days. Crystals were cryocooled as described above. C185A crystals belonged to space group $I4_1$ with one monomer in the asymmetric unit and a solvent content of 54.6% with the following unit cell dimensions: a = 86.28 Å, b = 86.28 Å, and c = 152.99 Å.

X-ray diffraction data were collected at the South East Regional Collaborative Access Team (SER-CAT) BM-22 beamline at the Advanced Photon Source (Argonne National Laboratory, Argonne, IL). All data sets were scaled and indexed using HKL2000 with DENZO and SCALEPACK (*31*). The structures were solved by molecular replacement using PHASER in the CCP4 suite of programs, utilizing the coordinates of wild-type rCSO residues 95−466 [Protein Data Bank (PDB) entry 2A99] as a search model, excluding the cofactor and solvent molecules (*32*). Iterative model building was performed using COOT (*33*) with PROBE (*34*) for visualization of all-atom contacts, and refinement was achieved with REFMAC (*35*). The stereochemistry of the structures was evaluated using MOLPROBITY (*36*) to assess the Ramachandran plots and atomic clash scores. For the structures reported in this study, TLS refinement was performed at the final stages of refinement (*37*), and water molecules were added to complete the models using COOT.

EXAFS and Near-Edge Data Collection on rCSO C185S and C185A. Samples of rCSO for XAS analysis were loaded into 2 mm × 10 mm × 10 mm lucite sample cuvettes, which were then frozen in liquid nitrogen (LN_2) and stored at LN_2 temperature until XAS measurements were taken. An additional C185S sample containing 20 mM sulfite was prepared.

XAS data were collected at SSRL with the SPEAR 3 storage ring operating between 90 and 100 mA at 3 GeV. Mo K-edge data were collected on beamline 7-3, from a 20-pole 2 T wiggler source with a downstream vertically collimating Rh-coated mirror and Si(220) double-crystal monochromator. Harmonic rejection was achieved via adjustment of the angle of the collimating mirror so that the harmonic fell above the cutoff. Beam intensity was monitored using argon-filled ion chambers. XAS was measured using the Mo $K\alpha_{12}$ fluorescence using a 30-element solid-state germanium array detector (*38*) through a Soller slit assembly and a zirconium filter with a thickness of 3 absorption units. Samples were maintained at 10 K using an Oxford Instruments helium flow cryostat. The energy was calibrated from the transmittance spectrum of a Mo foil collected simultaneously with sample fluorescence, and the lowest-energy inflection point was assumed to be 20003.9 eV. A total of eight scans were collected for the rCSO C185S mutant (k range to 17 $Å^{-1}$) and six scans for C185A (k range to 16 $Å^{-1}$). The energy threshold of the EXAFS region was assumed to be 20025.0 eV.

EXAFS Data Analysis. EXAFS oscillations, $\chi(k)$, were analyzed by curve fitting using EXAFSPAK[1] (e.g., ref *24*) with ab initio theoretical phase and amplitude functions calculated using FEFF version 8.25 (*39*, *40*). No smoothing, filtering, or other manipulations were performed on the data.

Density Functional Theory Calculations. Structure calculations of trioxo and dioxo Mo^{VI} complexes were performed without geometry or symmetry constraints using hybrid density functional method B3LYP, with the computational package Gaussian 03, revision E.01 (*41*). A mixed basis set approach was employed for geometry optimizations and subsequent harmonic frequency calculations, with LANL2DZ (*42*, *43*) used for the Mo atom, 6-31G(d) for C, O, N, and H atoms, and the larger 6-311+G(d,p) basis set for the S atoms. Structures were considered optimized when the change in energy between subsequent optimization steps fell below 0.03 kJ/mol.

Solvation effects were modeled with the integral equation formalism polarizable continuum model (IEFPCM) (*44*−*46*) with dielectric values representing water (ε = 78.39) or a lower dielectric representing a hydrophobic protein interior (approximated by ε = 4.00). In some instances, additional explicit water molecules or fragments of protein-derived side chains were included in some structure calculations to assess the effect of H-bonding interactions on the Mo^{VI} coordination geometry and Mo−ligand bond lengths.

RESULTS

Spectral Analysis of C185S and C185A rCSO. Previous site-directed mutational studies by Garrett and Rajagopalan had indicated that Cys207 in HSO played an important role in Mo coordination and hence the catalytic activity of SO (*22*). Kinetic and spectroscopic studies suggested functional and structural changes in the HSO C207S variant enzyme; however, it was unclear if perturbations of the macromolecular structure of the variant were present. Unfortunately, HSO has not produced high-quality crystals for diffraction to date. To further study the role of this conserved Cys in SO and to obtain detailed structural information, the analogous Cys → Ser mutation was generated in the highly homologous rCSO at the equivalent position, which has produced high-quality crystals for diffraction (*4*, *16*). The C185S variant and the C185A variant of rCSO were generated, expressed, and purified from *E. coli*. The TP1000 bacterial strain used for expression is deficient in the enzyme required to synthesize the guanine dinucleotide form of the Moco cofactor, utilized in *E. coli* molybdoenzymes (*47*). This mutation therefore results in the accumulation of Moco which is required by eukaryotic SO and results in the production of a high level of active, cofactor-containing enzyme. The protein behaved like wild-type rCSO throughout the purification, and the Mo contents of purified C185S and C185A were comparable. To determine if the C185S and C185A variants were capable of being reduced by sulfite, the spectra of both C185S and C185A were recorded in the as-purified oxidized state and in the presence of sulfite. Wild-type CSO exhibits different spectra in the oxidized and reduced form due to the change in oxidation of the heme group. The spectrum of the oxidized form of the variants is similar to that of wild-type rCSO (Figure 1a). The addition of sodium sulfite to a final concentration of 1 mM resulted in a spectrum similar to that of the oxidized wild-type enzyme, suggesting that the variants were not reduced and had not been able to oxidize sulfite to sulfate.

Kinetic Properties of the Mutants. Steady-state kinetic analysis of the C185S and C185A variants over the pH range of 6.0−10.0 revealed that compared to wild-type CSO, C185S and C185A had significantly diminished activity across the entire pH range. In both the C185S and C185A variants, there was very little SO activity as reported by cyt *c* reduction observed at 550 nm, and the resulting data gave poor fits to the Michaelis−Menten equation. These results suggested that both variants are incapable of transferring an electron from the heme to the physiological electron acceptor cyt *c*. To investigate if the variant enzymes were capable of oxidizing sulfite to sulfate in the presence of ferricyanide (a small molecule, nonspecific electron acceptor), the C185S and C185A variants were assayed for sulfite oxidase activity, which revealed that there was ∼1−2.5% activity relative to wild-type CSO at pH 7.0 and 0.05−0.09% activity at pH 8.5 (Figure 1b). These results suggest that the Mo centers of the C185S and C185A variants have significantly attenuated ability to oxidize sulfite to sulfate.

Structural Determination and Refinement. The structures of C185S, C185S_SO_3, and C185A (Figure 2a) variants were determined by molecular replacement. Initially, we attempted to use the coordinates from the full-length natively purified CSO (PDB entry 1SOX) as a search model; however, we were unable to obtain a search solution with all components. We then used the wild-type rCSO coordinates (rCSO, PDB entry 2a99, chain A monomer residues 95−466) as the search model. Despite the fact that the full-length proteins were used for crystallization and the crystals exhibited the red color characteristic of a heme prosthetic group, no difference electron density was observed for the N-terminal b_5-type cytochrome domain in any of the structures obtained, presumably because of the heme domain adopting multiple orientations within the crystal. These results were consistent with previously published results (*16*). C185S crystallizes in space group $C222_1$; the crystals of C185S_SO_3 and C185A belong to space group $I4_1$, and all crystals contain one monomer in the asymmetric unit as calculated by the Matthews coefficient (*48*). An attempt was made to obtain a substrate-bound crystal of C185S by soaking the C185S crystals in a mother liquor solution with 1 mM sodium sulfite, but the crystals appeared to dissolve or burst immediately upon its addition. The structure of C185S crystallized in the presence of sulfite contains one sulfite molecule per monomer. All structures have good stereochemistry,

[1] http://ssrl.slac.stanford.edu/exafspak.html.

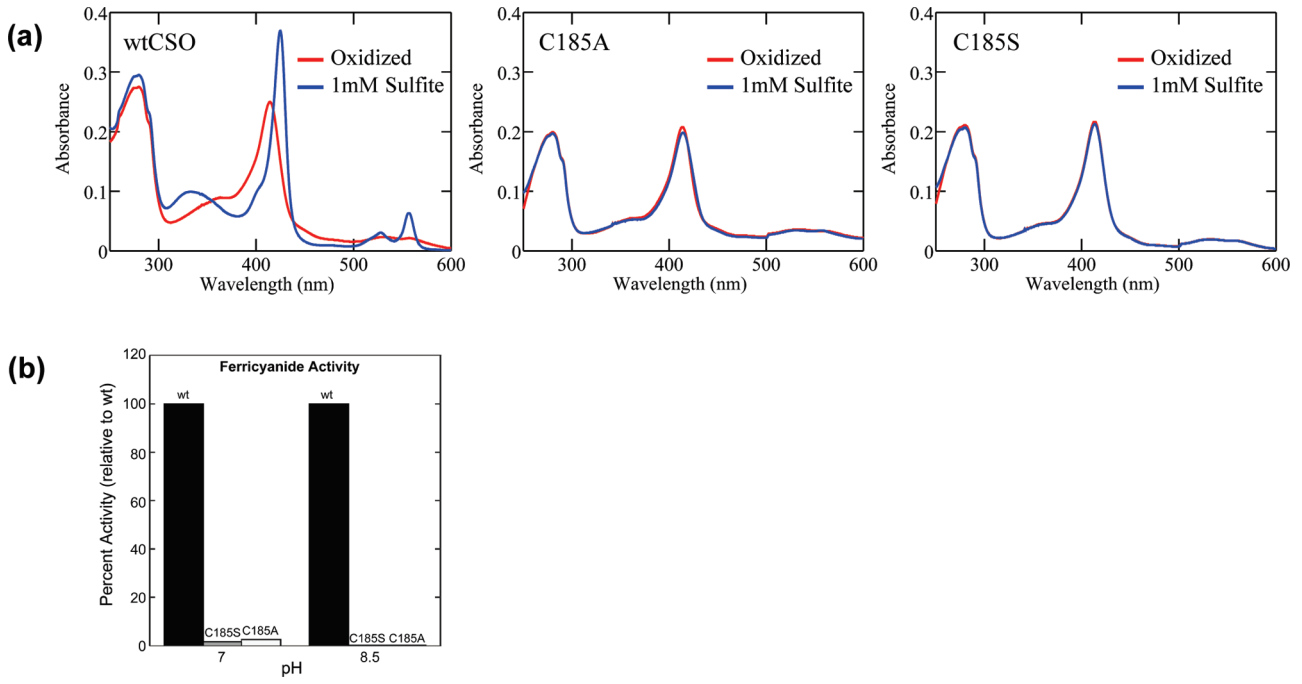

FIGURE 1: (a) UV−vis absorption spectra of CSO in the absence and presence of 1 mM sodium sulfite for CSO, C185A, and C185S. (b) Ferricyanide activity assays of rCSO, C185S, and C185A at pH 7 and 8.5.

with all residues in the most favored and additionally allowed regions of the Ramachandran diagram as determined by MOLPROBITY (*36*). Several cycles of least-squares minimization and model building resulted in structural models with the crystallographic R_{cryst} and R_{free} values reported in Table 1.

Structure of the C185S Variant and Comparison to rCSO. The structure of C185S was refined to 1.9 Å resolution, with an R_{cryst} of 0.18 and an R_{free} of 0.20. The topology of the protein fold of this variant is virtually identical to that of the natively purified enzyme shown in Figure 2a and consists of the central catalytic Moco-containing domain and the C-terminal dimerization domain. As reported previously, the SO catalytic core domain contains a unique fold consisting of nine α-helices and 13 β-strands divided into three β-sheets (*4*). The Moco is located deep in the core of this domain and is held in place by a network of hydrogen bonds and van der Waals interactions. The structure of the C-terminal dimerization domain contains two β-sheets comprised of seven β-strands arranged in a Greek key motif. The structures of C185S and rCSO are similar, as indicated by a root-mean-square deviation (rmsd) of 0.231 Å between Cα atoms for aligned residues.

The Moco was initially modeled into the structure containing the form of the cofactor seen in the wild-type rCSO structure with the pterin ring and two oxo ligands bound to the Mo atom as the initial model. While this led to a model that was in good agreement with the pterin ring of the cofactor, there was additional $F_o - F_c$ electron density present around the Mo for which the two oxo groups alone did not account.

Previous EXAFS studies on wild-type CSO indicated the oxidized form of the Mo center is coordinated by two oxo ligands and three sulfur ligands, whereas in the reduced form, only one oxo is observed (*49*, *50*). These early data had limited *k* range and signal-to-noise ratios, and a more accurate picture of the active site is that obtained from combined EXAFS and DFT analysis of human SO (*51*). This indicates that the oxidized Mo^{VI} enzyme possesses two Mo═O bonds of 1.72 Å and three Mo−S bonds of 2.41 Å, whereas the reduced Mo^{IV} enzyme possesses one Mo═O bond of 1.72 Å, two Mo−S bonds of 2.35 Å and one of 2.41 Å, and one Mo−OH_2 bond of 2.30 Å (*51*). In the crystal structure of CSO (*4*), the Mo center was found to possess the structure expected for the reduced Mo^{IV} or partially reduced Mo^{V} state, which was likely due to photoreduction while it was in the X-ray beam (*52*). To address the possibility of an additional oxygen in these data, the ligand was modeled as either an oxo or a hydroxyl ligand, with the oxo resulting in the best fit to the density. Previous EXAFS studies of the C207S variant of HSO indicated the presence of a third oxo ligand bound to the Mo atom (*23*, *24*), and this was modeled into the density for C185S with good agreement (Figure 2b).

Comparison of the active site residues of C185S with rCSO residues Arg138, Arg190, and Trp204 indicates that these residues in the C185S variant adopt analogous positions compared with those of the wild type. The Ser mutation adopts a conformation similar to that of the wild-type Cys at position 185; however, the distance from the Mo to the serine side chain is longer (3.55 Å) compared to the Cys−Mo distance of 2.47 Å (see Figure S1 of the Supporting Information). This longer distance argues against the Ser hydroxyl contributing as the third oxygen ligand to the Mo center. Surprisingly, in the structure of C185S in the absence of its substrate, no electron density was observed for the active site residue Tyr322 (Figure 3); furthermore, the entire loop region containing Tyr322 (residues 310−340) exhibited little electron density, except for seven residues (326−332) in the middle of the loop that adopted an alternate conformation relative to that of the wild-type protein. The residues in this loop region, with poorly defined or no electron density, were excluded from refinement. In a comparison of the active sites of the two structures, it is apparent that there is a conformational change of the Arg450 side chain, resulting in a more extended conformation that orients it outward from the active site. It is possible that the extended conformation as observed in the substrate free C185S variant is due to the missing Tyr322 side chain and/or alternate main chain interactions, allowing the Arg450 side chain to swing out and away from the active site.

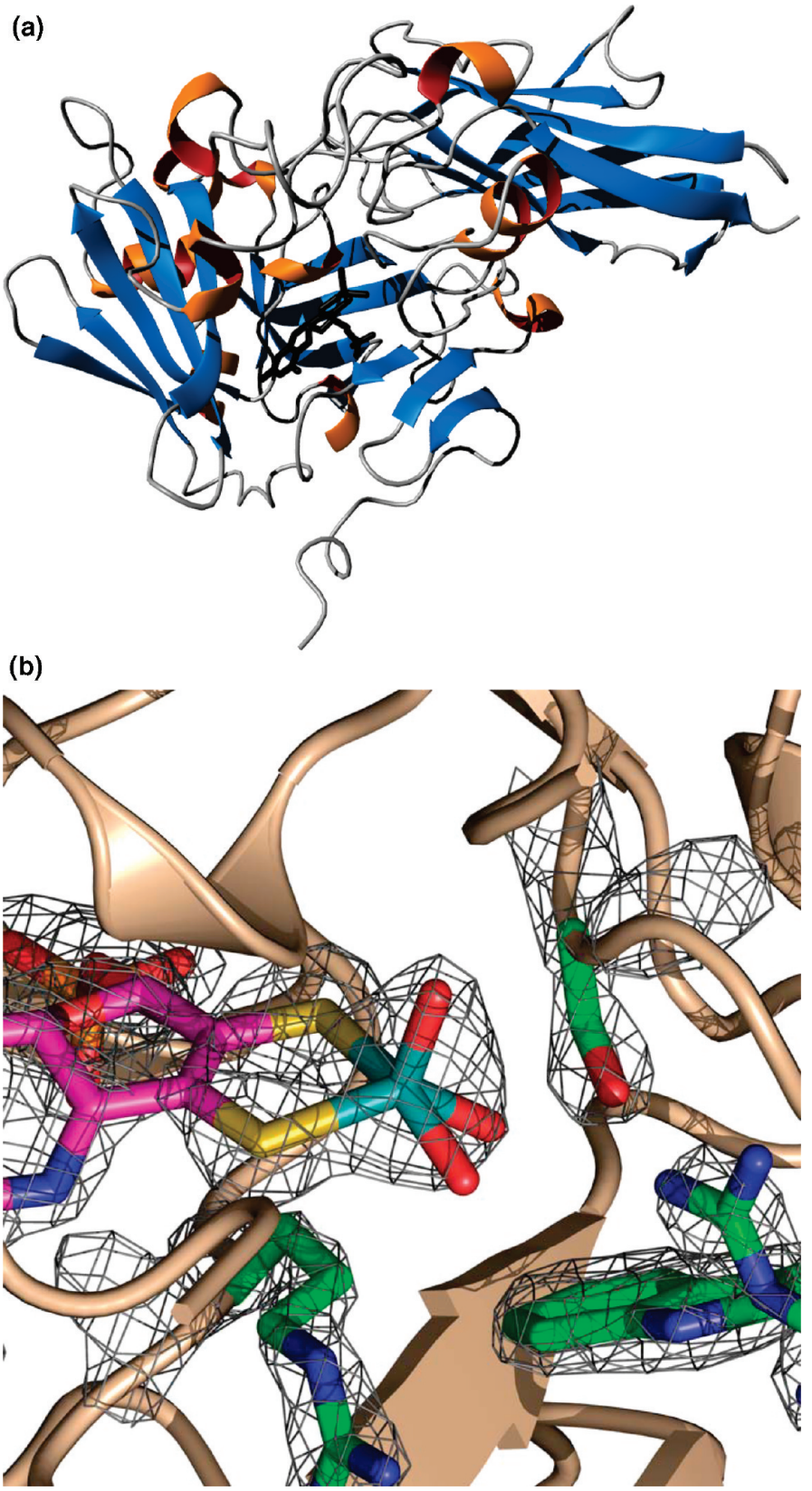

FIGURE 2: (a) Structure of the C185S variant of rCSO. The molybdopterin cofactor is represented in stick representation, and the main chain is shown in cartoon representation. (b) The $2F_o - F_c$ electron density map around the active site of C185S, illustrating the density corresponding to the three oxo groups.

Structure of C185S in the Presence of Sulfite. In an attempt to generate a substrate-bound form of the enzyme, the C185S variant was crystallized in the presence of sulfite. The resulting crystal structure is similar to the structure of rCSO with an rmsd of 0.186 Å for all Cα atoms relative to rCSO and an rmsd of 0.326 Å compared with C185S. Upon determination of the structure, additional electron density was observed close to the active site of the enzyme that was not present in the C185S

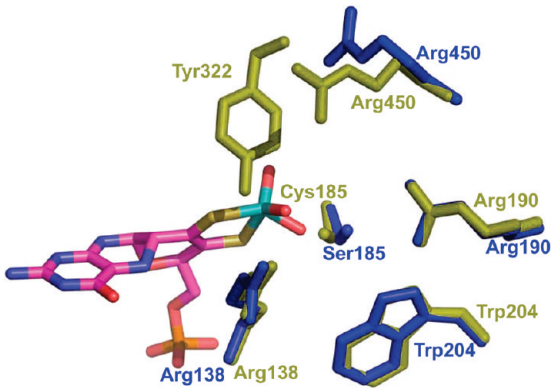

FIGURE 3: Overlay of active site residues of C185S in the absence of its substrate sulfite and rCSO. The side chains of rCSO are colored yellow, and the side chains of C185S are colored blue. Only the Moco of C185S is shown.

Table 1: Crystallographic Data and Refinement Statistics

	C185S	C185S_SO$_3$	C185A
resolution (Å)	50−1.9	50−2.4	50−2.8
wavelength (Å)	0.9765	1.00	1.00
space group	$C222_1$	$I4_1$	$I4_1$
cell constants (Å)	$a = 86.46$	$a = 86.28$	$a = 86.28$
	$b = 131.51$	$b = 86.28$	$b = 86.28$
	$c = 98.88$	$c = 152.33$	$c = 152.99$
no. of molecules in the asymmetric unit	1	1	1
total no. of observations	312655	144687	76652
no. of unique reflections	43889	21565	13652
mean redundancy	7.1 (5.3)	6.8 (5.6)	5.6 (5.2)
R_{sym}[a] (%)	5.6 (26.3)	8.2 (37.2)	4.6 (24.2)
completeness (%)	98.1 (85.6)	99.4 (95.4)	99.3 (94.3)
mean I/σ	50.6 (4.6)	30.9 (3.4)	27.7 (4.7)
R_{cryt}[b] (%)	18.8	18.1	17.1
R_{free}[c] (%)	20.8	20.8	22.4
mean B factor (Å^2)	22.7	38.7	20.7
no. of atoms used in refinement	2951	2994	2940
no. of waters	201	83	43
root-mean-square deviation for bond lengths (Å)	0.008	0.008	0.014
root-mean-square deviation for bond angles (deg)	1.12	1.21	1.64
Ramachandran statistics[d]	98.3/1.7	98.4/1.6	97.3/2.7

[a] $R_{sym} = \sum_{hkl}\{\sum|I - \langle I\rangle|/\sum\langle I\rangle\}$, where I is the observed intensity and $\langle I\rangle$ is the average intensity of multiple symmetry-related observations of that reflection. [b] $R_{cryst} = \sum(|F_o| - |F_c|)/\sum|F_o|$, where F_o and F_c are the observed and calculated structure factors, respectively. [c] R_{free} is the R factor based on the data with withheld at random from structural refinement. [d] Ramachandran statistics represent favored and allowed regions, with no outliers.

structure. As the crystallization conditions for C185S with sulfite were nearly identical to the conditions used for C185S obtained in the absence of sulfite, we concluded that the additional density is likely attributable to a sulfite molecule in the active site. The sulfite is bound by a network of hydrogen bonds that holds the sulfite S atom close to the Mo center, which may be mechanistically relevant to the active form of the enzyme (Figure 4a). In the presence of sulfite, the active site residue Tyr322 adopts a conformation similar to that of rCSO, as does the loop region (residues 311−339) that had adopted an alternate conformation in the structure of C185S grown in the absence of sulfite. The position of the sulfite in the C185S variant is very similar to that

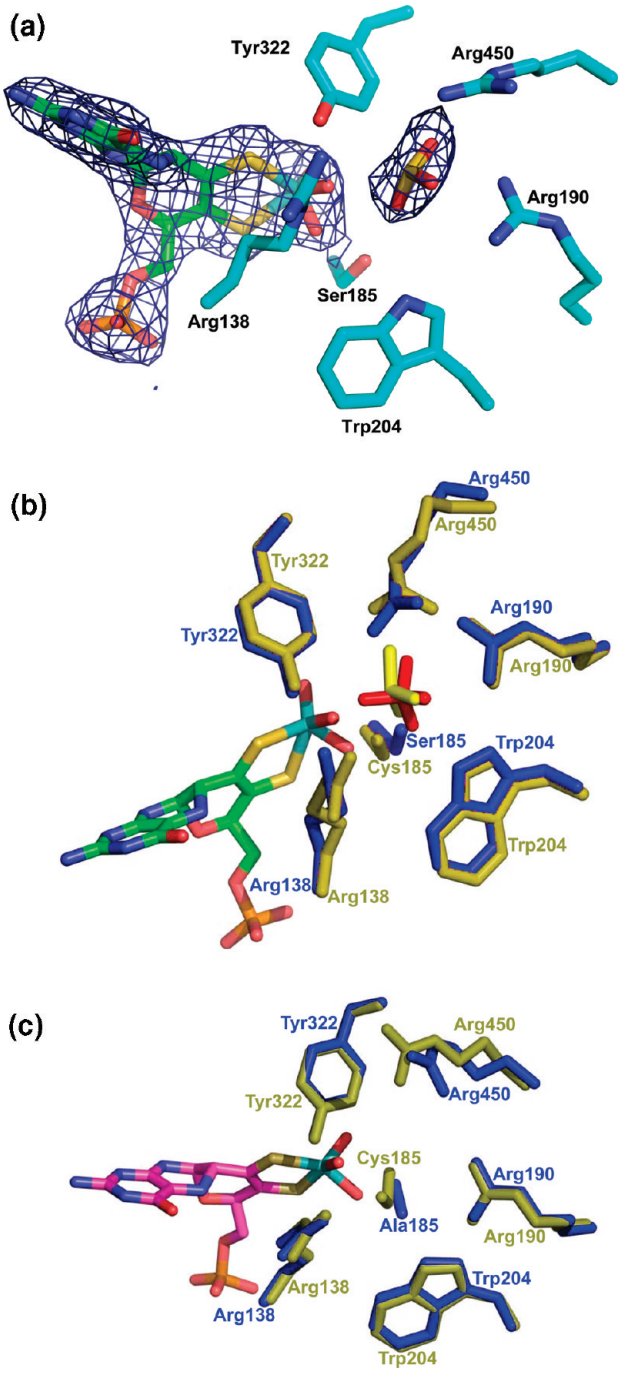

FIGURE 4: (a) $2F_o - F_c$ electron density map of the active site of C185S with bound sulfite. The active site is colored cyan, while the sulfite is colored red and yellow. Electron density around the Moco and the sulfite is shown. (b) Overlay of the active site of rCSO with sulfate and C185S with sulfite. The active site residue side chains are colored blue (C185S) or yellow (rCSO). Only the C185S Moco is shown. The sulfite present in C185S is colored yellow, and the sulfate of rCSO is colored red. (c) Active site overlay of rCSO and C185A. The active site of rCSO is colored yellow, and the active site of C185A is colored blue. Only the Moco of C185A is shown.

of the sulfate bound in the active site of rCSO. Upon overlaying the C185S_SO$_3$ structure with the structure of rCSO with sulfate bound in the active site (PDB entry 2A9A), we find the positions of the sulfite and sulfate are nearly identical (Figure 4b). Additionally, it is apparent that the active site side chains for residues Arg138, Arg190, and Trp204 adopt conformations similar to that of the rCSO bound to sulfate, and the Ser185 side chain appears to adopt a conformation identical to that of the protein

crystallized in the absence of sulfate. Furthermore, Arg450 adopts a conformation similar to that of rCSO crystallized in the presence of sulfate where the guanidine moiety of the side chain is directed into the active site of the enzyme. The substrate-induced conformational change of Arg450 by sulfite is analogous to the sulfate-induced conformational change of Arg450, reported for the rCSO structure (*4*).

Structure of the C185A Variant of rCSO and Comparison to rCSO. The structure of the C185A variant of rCSO is similar to that of wild-type rCSO, with an overall rmsd of 0.2 Å using the Cα atoms of rCSO (PDB entry 2A99). We also observed the presence of a glycerol molecule in the active site of the mutant at the same position as the sulfate in the rCSO structure. Initially, the dioxo form of the Mo center was modeled into the C185A active site, with good agreement. From visual inspection of the electron density maps, however, it was apparent that there was additional $F_o - F_c$ electron density present around the Mo center for which the two oxo groups did not account, indicating that the Mo of the C185A variant is also in the trioxo form, and this form was subsequently used for further structure refinement. In general, the side chain residues in the C185A variant active site adopt conformations similar to those in the rCSO active site, with the exception of Ala185 and Arg450. In the C185A active site, the Ala185 side chain is pointed away from the active site, indicating that the nonpolar side chain does not interact with the polar active site environment (Figure 4c). The Arg450 residue also adopts a conformation slightly different from that in the wild-type enzyme, which can be attributed to the larger glycerol molecule in the C185A active site.

Deposition of Atomic Coordinates and Structural Factors. The atomic coordinates and structural factors (PDB entries 3HBG, 3HBP, and 3HBQ) have been deposited in the Protein Data Bank, Research Collaboratory for Structural Bioinformatics, Rutgers University, New Brunswick, NJ (http://www.rcsb.org/).

EXAFS Analysis of the Molybdenum Center of the C185S and C185A Variants of rCSO. To further investigate the nature of the molybdenum coordination environment and to confirm the interpretation of the crystallographic data which show that the molybdenum of the Moco is bound to three oxo groups in both variants, EXAFS experiments were performed on the C185S and C185A variants of rCSO and further supplemented by DFT structure calculations.

Molybdenum K-Edge Near-Edge Spectra. Figure 5 shows the Mo K-edge near-edge region of the C185S and C185A variants. Both CSO mutants exhibit essentially identical near-edge features, indicating similar active site environments in both; their close similarity is further apparent in the inset plot of the first derivative of the near-edge region.

Both C185S and C185A have a pronounced pre-edge feature in the near-edge spectrum, at approximately 20008 eV, attributable to a Mo=O group. This feature arises from a formally dipole forbidden 1s → 4d bound-state transition into π^* orbitals oriented along the Mo=O bond vectors (*24*, *53*, *54*), and these oxo-edge features are more pronounced than those observed in the dioxo Mo^{VI} form of CSO (*24*).

Molybdenum K-Edge EXAFS Spectra. Figure 6a shows the EXAFS spectra for the C185S and C185A mutants, as well as the Fourier transform of each (Figure 6b), along with the best fits to the data. The Fourier transform (Figure 6b) is dominated by two main backscattering interactions, with a major transform peak at an $R + \Delta$ of ~1.8 Å and a second smaller transform peak

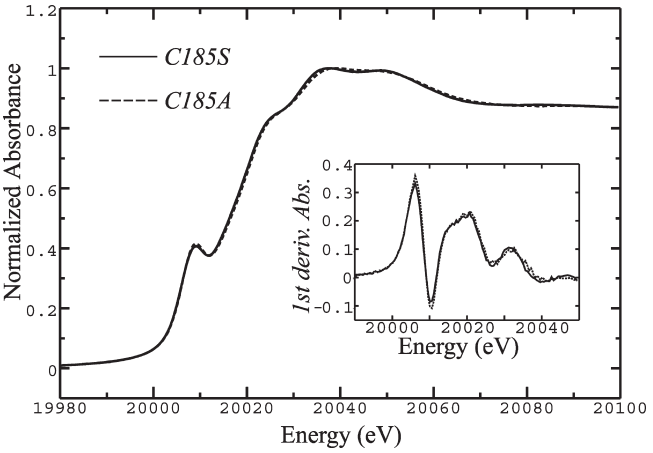

FIGURE 5: Mo K-edge near-edge spectra for rCSO mutants C185S (—) and C185A (---). The inset shows the expanded first derivative of the near-edge region.

at an $R + \Delta$ of ~2.4 Å, which are assigned to Mo=O and Mo−S groups, respectively. EXAFS curve fitting analysis of the C185S and C185A mutants (shown in Table 2) reveals both contain essentially the same coordination environment, with three Mo=O ligands at 1.75 Å and two Mo−S ligands between 2.47 and 2.48 Å.

Trioxo Mo^{VI} DFT Structure Calculations. Representative structures from DFT calculations on a trioxo Mo^{VI} model of CSO as well as a structure previously characterized by X-ray crystallography (*55*) are shown in Figure 7, and a full summary of calculated structure data is given in Table S1 of the Supporting Information. Geometry optimizations on trioxo-benzenedithiolato-molybdenum(VI) (**1**) yield approximately square pyramidal coordination geometries, in agreement with experimental data (*55*), and analogous results were obtained for **2**, which is a model of the SO active site. Structure optimizations of hydroxyl-bound dioxo Mo^{VI} complexes give Mo−O (H) bond lengths that are ~0.2 Å longer than those of analogous trioxo Mo^{VI} complexes (data not shown), demonstrating that the presence of hydroxyl substituents would be clearly visible in the EXAFS Fourier transform at the current resolution for both C185S and C185A. While optimizations in the gas phase provide trioxo Mo=O distances comparable with experimental data ($Mo=O_{apical}$ distances of 1.749 and 1.733 Å and $Mo=O_{equatorial}$ distances of 1.760, 1.754, and 1.757 Å in the crystal structure), the Mo−S ligands, however, optimize to significantly longer distances of ~2.70 Å, compared with 2.54 and 2.56 Å in the crystal structure (*55*) or ~2.475 Å from EXAFS (see Table 2).

Performing the geometry optimizations in the presence of a polarizable continuum has a negligible effect on Mo=O ligand distances but results in a decrease in the Mo−S distance of ~0.095 Å in a protein-like environment ($\varepsilon = 4$) and ~0.08 Å in a water-like continuum ($\varepsilon = 78.39$). While the lower dielectric value is treated as being indicative of the hydrophobic interior of most proteins, the SO active site is considerably more polar. In the wild-type enzyme, the Mo active site has an overall charge of −1 and is immediately adjacent to a cationic Arg and a polar Tyr. Furthermore, the channel leading to the active site from the protein exterior is lined by charged and polar residues, such as Arg, Asn, Asp, Gln, Lys, and Ser, and the channel is filled with numerous water molecules. There are two charged and six polar residues within 10 Å of the active site, not counting exposed protein backbone atoms from residues such as Cys185, Ala186,

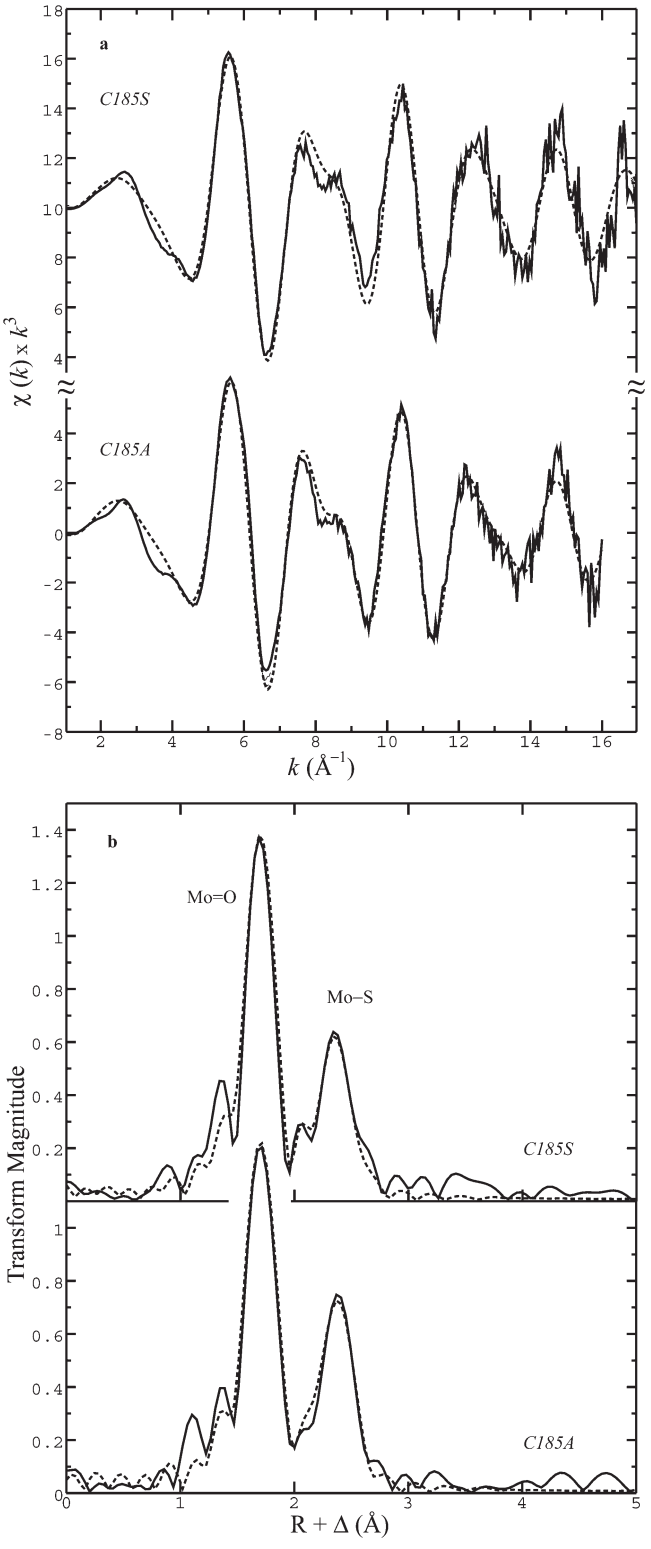

FIGURE 6: (a) Molybdenum EXAFS oscillations of oxidized C185S and C185A mutants of CSO. (b) Fourier transforms of the EXAFS data are phase corrected for Mo−O backscattering. Solid lines show experimental data, and dashed lines show the best fit from parameters in Table 2 (shown in bold).

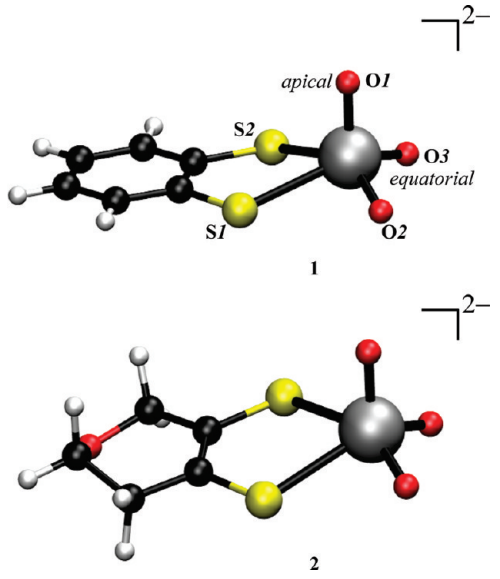

FIGURE 7: Representative structures of (**1**) trioxo-benzenedithiolato-molybdenum(VI) and (**2**) trioxo(2,3-dihydro-2*H*-pyran-4,5-dithiolato)molybdenum(VI) models used in DFT structure calculations. Structures shown correspond to the optimized geometries from the gas phase. Structures optimized in the presence of a polarizable continuum do not significantly differ structurally except in their Mo−S bond lengths and are therefore not shown.

Table 2: EXAFS Curve Fitting Results[a]

Mo−O			Mo−S				
N	*R* (Å)	σ^2 (Å^2)	*N*	*R* (Å)	σ^2 (Å^2)	ΔE_0 (eV)	error
				C185S			
2	1.753(2)	0.0018(1)	3	2.470(4)	0.0075(3)	−14.1(7)	0.305
3	**1.753(1)**	**0.0033(1)**	**2**	**2.470(2)**	**0.0049(2)**	**-13.9(5)**	**0.237**
3	1.755(2)	0.0033(1)	3	2.472(3)	0.0073(2)	−13.7(6)	0.274
3	1.755(2)	0.0033(1)	1	2.45(2)	0.0035(6)	−13.5(6)	0.237
			1	2.50(2)	0.005(2)		
				C185A			
2	1.747(2)	0.0012(1)	3	2.468(4)	0.0081(3)	−16.0(7)	0.286
3	**1.748(2)**	**0.0028(1)**	**2**	**2.469(3)**	**0.0058(3)**	**-15.2(6)**	**0.253**
3	1.748(2)	0.0028(1)	3	2.468(4)	0.0080(2)	−15.7(6)	0.275
3	1.749(2)	0.0028(1)	1	2.44(3)	0.004(2)	−15.3(7)	0.258
			1	2.50(4)	0.005(3)		

[a]Best fits to the data are shown in bold. Coordination numbers, *N*, interatomic distances, *R*, Debye−Waller factors, σ^2, and threshold energy shifts, ΔE_0. Values in parentheses are the estimated standard deviations (precisions) obtained from the diagonal elements of the covariance matrix. The accuracies will be much greater than these values and are generally accepted to be ±0.02 Å for bond lengths and ±20% for coordination numbers and Debye−Waller factors. The fit-error function is defined as $F = [\sum k^6(\chi_{calcd} - \chi_{expt})^2/\sum \chi_{expt}^2]^{1/2}$, where the summations are over all data points included in the refinement.

and Ala297, which can form H-bonds with the apical oxo group in the active site. In addition, the more anionic trioxo form of the active site in the C185 mutants (its formal charge is −2) argues for stronger charge−charge and H-bonding interactions with the active site and argues against using a lower dielectric constant for implicitly representing the active site environment. The Mo−ligand bond lengths from the water-like continuum model agree (at least qualitatively in the case of Mo−S ligands) with EXAFS curve fitting analysis of Mo−ligand distances listed in Table 2.

Inclusion of secondary solvation shell waters, H-bonded to apical atom O1 and equatorial atom O2 (numbering shown in Figure 7), a model of active site residues such as CH_3OH (representing the Ser side chain) H-bonded to equatorial atom O3, and a model for the Arg138 side chain H-bonded to

equatorial atom O1 gives significantly reduced Mo−S bond lengths when optimized in the presence of a water-like polarizable continuum. With this model, the Mo=O bond lengths are minimally perturbed; however, the Mo−S bonds in structure **2** are significantly improved, but still longer than indicated from EXAFS curve fitting (ΔMo−S = 0.091 Å) or crystallography (ΔMo−S = 0.021 Å).

A detailed summary of computational results is contained in Table S1 of the Supporting Information.

DISCUSSION

Photoreduction of transition metal sites during X-ray diffraction data acquisition is a common problem among metalloproteins. SO appears to be particularly susceptible to this, and aside from this work, there are no reported structures in which the active site is not photoreduced. Photoreduction of Mo enzymes will give rise to distortions in the Mo coordination environment as a result of mixed oxidation states and coordination geometries in the diffracting crystal. The Cys mutants of CSO are remarkable in that they are resistant to photoreduction, and to reduction in general (*23*), and the crystal structures reported here are the first SO structures of a bona fide oxidized Mo^{VI} SO.

Previous site-directed mutagenesis studies had identified that the C207S mutation in HSO dramatically decreases enzymatic activity (*23*), and spectroscopic studies suggested a change in the ligand coordination environment of the active site to a highly oxidized trioxo form (*24*). Initially, it was unclear if the loss of activity in the C207S variant of HSO was solely due to the change in coordination at the Mo center, or if there were other macromolecular structural perturbations that could not be observed by either UV−visible spectroscopic or EXAFS techniques. To address these questions, structural studies in conjunction with biochemical and spectroscopic studies were pursued. To date, the HSO Moco domain has proven to be difficult to crystallize, whereas the highly homologous CSO has proven to be amenable to crystallization. For this reason, recombinant CSO was used for the structure−function studies presented in this work.

Both the C185S and C185A variants of rCSO are catalytically inactive and are subsequently unable to reduce cyt *c*. No catalytic activity was observed above that of the cyt *c* background for the C185S or C185A variant over a range of pH values. In wild-type CSO, in the absence of cyt *c*, there is a pronounced change in the absorption of the oxidized heme domain at 413 nm and the reduced heme domain with an absorption shift to 426 nm (*29*). In the UV−visible spectral analysis of both C185S and C185A (Figure 1a), there is no shift in this peak between the as-purified C185S or in the presence of 1 mM sodium sulfite, suggesting that the heme domain is not reduced following oxidation of sulfite. To further address whether the active site of C185S or C185A could reduce sulfite to sulfate, the small molecule electron acceptor ferricyanide was used. Ferricyanide activity assays of rCSO, C185S, and C185A (Figure 1b) indicate that the C185S and C185A variants have ∼1−2.5% of the activity of rCSO at pH 7.0 and <1% of the activity of rCSO at pH 8.5, conclusively demonstrating that both C185S and C185A have negligible catalytic activity.

The most probable explanation for the observed loss of activity is an increased reduction potential for the Mo-containing active site. The formal charge of the wild-type active site is −1, which must coordinate the anionic substrate and accept electrons (with transfer of an O atom) during catalysis. In the C185S and C185A mutants, the replacement of the Cys S donor atom with an additional oxo ligand results in an active site with a formal charge of −2, which will be more difficult to reduce during catalysis. While UV−visible spectroscopic and kinetic characterizations reveal the effects of the C185S and C185A mutations on enzyme function, questions remain about the effect these mutations might have on the overall structure of the active site.

Crystallographic analysis of C185S indicates that while the overall fold of the variant is similar to that of the wild-type enzyme there are some significant changes between the two in the active site. Most notable is the disordered loop region from residue 310 to 340, which displayed little to no electron density, and the active site residue Tyr322 is completely absent from the active site in this structure. The change in the Mo coordination environment also appears to change the local environment of the active site, resulting in the disordered loop in conjunction with a loss of catalytic activity. It has been hypothesized that Tyr322 plays an important role in substrate binding and catalysis (*26*).

Significant changes in the Mo coordination environment of the mutant enzymes can be observed. In wild-type SO, three sulfurs coordinate the Mo atom, one from the side chain of Cys185 and two from the dithiolene of the molybdopterin cofactor. Two oxo groups contribute to the final approximately square pyramidal coordination of the Mo center of SO. Previous EXAFS studies of SO have indicated the presence of two oxo ligands at a distance of 1.72 Å from the Mo in the oxidized Mo^{VI} form, while the reduced Mo^{IV} form of the enzyme contains one oxo ligand and a hydroxyl bound to the Mo center at a distance of 2.30 Å (*51*). Further EXAFS studies of the HSO C207S variant indicated the presence of a novel trioxo active site (*24*), supporting the C185S results reported herein. The structure of the wild-type CSO, although purified as the oxidized Mo^{VI} enzyme, was found to be in a reduced form in the crystal structure (*4*), most likely due to photoreduction during the acquisition of X-ray data (*4*, *52*).

The structure of the C185S variant crystallized in the presence of its substrate sulfite is similar to the structure of rCSO bound to sulfate with an rmsd of 0.186 Å for all Cα atoms. The reappearance of electron density for the active site residue Tyr322 and density for the loop region containing Tyr322 upon addition of sulfite were also observed. The proximity of the sulfite to the equatorial oxo group of the active site suggests that this may be the arrangement of the active site after the substrate binds but before its oxidation occurs. Because of charge repulsion between the guanidine moieties of Arg138 and Arg450, it has been proposed that Arg450 is not present in the active site in the oxidized form of the enzyme, and only upon binding of the negatively charged sulfite does Arg450 become attracted to the active site (*16*).

The structure of the C185A variant of rCSO is similar to that of the sulfate-bound form of rCSO, and a glycerol molecule is also observed in the active site of the C185A variant. The electron density around the Mo atom in C185A also suggests the presence of an additional oxo ligand. An interesting observation involved the active site reside Tyr322, which is disordered in the absence of sulfite in the C185S structure but has defined electron density in the C185A structure. It is possible that the Ser side chain adds to the volume of the active site and sterically hinders Tyr322 from entering, whereas the smaller methyl side chain of the Ala variant, which is also oriented away from the active site, does not lead to crowding of Tyr322 in the absence of sulfite. On the basis of the C185S and C185A active site structures, one may speculate that the Tyr322 residue is only present in a defined position in the active site when a favorable coordination to the substrate is possible.

The replacement of a sulfur ligand with the more electronegative oxygen preserves the square pyramidal geometry around the Mo center but results in loss of catalytic activity. The altered ligand sphere and charge of the trioxo site also significantly alter both the $Mo^{VI}-Mo^{V}$ and $Mo^{V}-Mo^{IV}$ redox potentials (*23*), which explains the lack of change in the spectroscopic signal of the C185S and C185A variants upon addition of sulfite, vis-à-vis the dramatic change in the rCSO spectrum upon addition of sulfite. The distance from the Mo to the hydroxyl oxygen of the Ser side chain in the C185S mutant is approximately 3.6 Å, compared to the wild-type Mo to Cys S atom distance of ~2.5 Å. This distance precludes a direct ligation of Ser to the Mo center.

While the crystal structure data are compelling, the 1.9 Å resolution is too low to infer the chemical species of the O donor atom in the active site environment, therefore making determination of the oxidation state from the crystallographic structure data alone problematic. To obtain more accurate quantitative information about the Mo coordination environment, EXAFS experiments were conducted on both rCSO variants.

The X-ray absorption pre-edge spectrum for both C185S and C185A exhibited a distinct oxo-edge effect, attributable to the Mo=O bond (Figure 5). The broad Fourier transform peak attributed to the Mo−S bond in the C185S mutant (Figure 6b) may be indicative of dissimilar Mo−S bond lengths. The EXAFS data can be fit to one shorter Mo−S ligand at 2.427 Å and one longer Mo−S ligand at 2.511 Å (σ^2 for each shell is 0.00362). However, this separation in Mo−S bond lengths ($\Delta R = 0.084$ Å) is below the resolution limit (approximated by $\Delta R = \pi/2 \times \Delta k$) of the EXAFS data (*51*) for C185S (0.098 Å). The resolution of the C185A data is slightly lower ($\Delta R = 0.105$ Å), making comparisons between differential Mo−S interactions less viable. Likewise, for Mo=O ligands, there is expected to be a small difference between the apical and equatorial Mo=O bond lengths in a square pyramidal environment; however, as we will discuss below, the predicted difference is less than 0.02 Å and well beyond EXAFS resolution limits.[2]

The analogous C185S mutant of CSO has previously been characterized for the HSO C207S mutant (*23*, *24*). EXAFS characterization of HSO C207S revealed the presence of trioxo coordination, with three Mo=O ligands at 1.744 Å and two Mo−S ligands at 2.473 Å. In a comparison of curve fitting analysis of the Ser mutants of CSO and HSO, the Mo=O ligands differ by ~0.01 Å while the Mo−S ligands differ by ~0.002 Å, indicating good agreement. These slight apparent differences between the trioxo coordination environments may be due to the EXAFS curve fitting analysis or subtle structural differences within the surrounding active site environment of the enzymes.

Computational results indicate that the mixture of hard oxo and soft thiolato ligands in the trioxo−Mo^{VI} complexes (**1** and **2** in Figure 7) is a structurally challenging coordination environment for the DFT methods employed. The Mo−S bond lengths of these structures are significantly affected upon going from the gas phase to a polarizable continuum.

We have shown that the conserved active site Cys of SO is essential for catalytic activity. The two mutants, C185S and C185A, exhibited severely attenuated activity using either the physiological electron acceptor, cyt *c*, or a nonspecific acceptor, ferricyanide. The crystal structures of the C185S and C185A variants indicate that the ligand environment of the Mo center contained an additional oxo group, replacing the S donor atom from Cys185. Our results also suggest that Tyr322 and Arg450 may play a role in substrate binding and turnover in SO. EXAFS and near-edge analysis confirmed that the Mo sites are in a highly oxidized trioxo form. DFT calculations on model trioxo−Mo^{VI} complexes generally gave good agreement with respect to Mo−ligand bond lengths and coordination geometries when the structures were optimized in the presence of a polar (water-like) dielectric with multiple stabilizing H-bond partners.

[2]A resolution of 0.02 Å would require collection of data with an unrealistic *k* range of 80 $Å^{-1}$.

ACKNOWLEDGMENT

We thank Dr. Margot W. Wuebbens for editing assistance and for helpful discussions and Mr. Graham Alexander and Ms. Ashley Carpenter for technical assistance with cloning and protein purification. SSRL is supported by the DOE OBES and OBER and by the NIH NCRR BTP.

SUPPORTING INFORMATION AVAILABLE

Mo−ligand bond lengths from DFT structure calculations (Table S1) and a structure overlay of the rCSO and C185S Mo coordination environments showing the difference in Mo−S(Cys) and Mo···O(Ser hydroxyl) distances (Figure S1). This material is available free of charge via the Internet at http://pubs.acs.org.

REFERENCES

1. Johnson, J. L., Hainline, B. E., and Rajagopalan, K. V. (1980) Characterization of the molybdenum cofactor of sulfite oxidase, xanthine oxidase, and nitrate reductase. Identification of a pteridine as a structural component. *J. Biol. Chem. 255*, 1783–1786.
2. Johnson, J. L., Hainline, B. E., Rajagopalan, K. V., and Arison, B. H. (1984) The pterin component of the molybdenum cofactor. Structural characterization of two fluorescent derivatives. *J. Biol. Chem. 259*, 5414–5422.
3. Cohen, H. J., Fridovich, I., and Rajagopalan, K. V. (1971) Hepatic sulfite oxidase. A functional role for molybdenum. *J. Biol. Chem. 246*, 374–382.
4. Kisker, C., Schindelin, H., Pacheco, A., Wehbi, W. A., Garrett, R. M., Rajagopalan, K. V., Enemark, J. H., and Rees, D. C. (1997) Molecular basis of sulfite oxidase deficiency from the structure of sulfite oxidase. *Cell 91*, 973–983.
5. Feng, C., Kedia, R. V., Hazzard, J. T., Hurley, J. K., Tollin, G., and Enemark, J. H. (2002) Effect of solution viscosity on intramolecular electron transfer in sulfite oxidase. *Biochemistry 41*, 5816–5821.
6. Johnson, J. L., Waud, W. R., Rajagopalan, K. V., Duran, M., Beemer, F. A., and Wadman, S. K. (1980) Inborn errors of molybdenum metabolism: Combined deficiencies of sulfite oxidase and xanthine dehydrogenase in a patient lacking the molybdenum cofactor. *Proc. Natl. Acad. Sci. U.S.A. 77*, 3715–3719.
7. Garrett, R. M., Johnson, J. L., Graf, T. N., Feigenbaum, A., and Rajagopalan, K. V. (1998) Human sulfite oxidase R160Q: Identification of the mutation in a sulfite oxidase-deficient patient and expression and characterization of the mutant enzyme. *Proc. Natl. Acad. Sci. U.S.A. 95*, 6394–6398.
8. Schindelin, H., Kisker, C., and Rajagopalan, K. V. (2001) Molybdopterin from molybdenum and tungsten enzymes. *Adv. Protein Chem. 58*, 47–94.
9. Dublin, A. B., Hald, J. K., and Wootton-Gorges, S. L. (2002) Isolated sulfite oxidase deficiency: MR imaging features. *Am. J. Neuroradiol. 23*, 484–485.
10. Rupar, C. A., Gillett, J., Gordon, B. A., Ramsay, D. A., Johnson, J. L., Garrett, R. M., Rajagopalan, K. V., Jung, J. H., Bacheyie, G. S., and Sellers, A. R. (1996) Isolated sulfite oxidase deficiency. *Neuropediatrics 27*, 299–304.
11. Bailey, J. L., and Cole, R. D. (1959) Studies on the reaction of sulfite with proteins. *J. Biol. Chem. 234*, 1733–1739.
12. Feng, C., Tollin, G., and Enemark, J. H. (2007) Sulfite oxidizing enzymes. *Biochim. Biophys. Acta 1774*, 527–539.
13. Garrett, R. M., Bellissimo, D. B., and Rajagopalan, K. V. (1995) Molecular cloning of human liver sulfite oxidase. *Biochim. Biophys. Acta 1262*, 147–149.

14. Garrett, R. M., and Rajagopalan, K. V. (1994) Molecular cloning of rat liver sulfite oxidase. Expression of a eukaryotic Mo-pterin-containing enzyme in *Escherichia coli*. *J. Biol. Chem. 269*, 272–276.
15. Neame, P. J., and Barber, M. J. (1989) Conserved domains in molybdenum hydroxylases. The amino acid sequence of chicken hepatic sulfite oxidase. *J. Biol. Chem. 264*, 20894–20901.
16. Karakas, E., Wilson, H. L., Graf, T. N., Xiang, S., Jaramillo-Busquets, S., Rajagopalan, K. V., and Kisker, C. (2005) Structural insights into sulfite oxidase deficiency. *J. Biol. Chem. 280*, 33506–33515.
17. Hiller, L. D.; et al. (2004) Sequence and comparative analysis of the chicken genome provide unique perspectives on vertebrate evolution. *Nature 432*, 695–716.
18. Banks, G. R., Shelton, P. A., Kanuga, N., Holden, D. W., and Spanos, A. (1993) The *Ustilago maydis* nar1 gene encoding nitrate reductase activity: Sequence and transcriptional regulation. *Gene 131*, 69–78.
19. Johnstone, I. L., McCabe, P. C., Greaves, P., Gurr, S. J., Cole, G. E., Brow, M. A., Unkles, S. E., Clutterbuck, A. J., Kinghorn, J. R., and Innis, M. A. (1990) Isolation and characterisation of the crnA-niiA-niaD gene cluster for nitrate assimilation in *Aspergillus nidulans*. *Gene 90*, 181–192.
20. Crawford, N. M., Smith, M., Bellissimo, D., and Davis, R. W. (1988) Sequence and nitrate regulation of the *Arabidopsis thaliana* mRNA encoding nitrate reductase, a metalloflavoprotein with three functional domains. *Proc. Natl. Acad. Sci. U.S.A. 85*, 5006–5010.
21. Crawford, N. M., Campbell, W. H., and Davis, R. W. (1986) Nitrate reductase from squash: cDNA cloning and nitrate regulation. *Proc. Natl. Acad. Sci. U.S.A. 83*, 8073–8076.
22. Garrett, R. M., and Rajagopalan, K. V. (1996) Site-directed mutagenesis of recombinant sulfite oxidase: Identification of cysteine 207 as a ligand of molybdenum. *J. Biol. Chem. 271*, 7387–7391.
23. George, G. N., Garrett, R. M., Prince, R. C., and Rajagopalan, K. V. (2004) Coordination chemistry at the molybdenum site of sulfite oxidase: Redox-induced structural changes in the cysteine 207 to serine mutant. *Inorg. Chem. 43*, 8456–8460.
24. George, G. N., Garrett, R. M., Prince, R. C., and Rajagopalan, K. V. (1996) The Molybdenum Site of Sulfite Oxidase: A Comparison of Wild-Type and the Cysteine 207 to Serine Mutant Using X-ray Absorption Spectroscopy. *J. Am. Chem. Soc. 118*, 8588–8592.
25. Feng, C., Wilson, H. L., Hurley, J. K., Hazzard, J. T., Tollin, G., Rajagopalan, K. V., and Enemark, J. H. (2003) Role of conserved tyrosine 343 in intramolecular electron transfer in human sulfite oxidase. *J. Biol. Chem. 278*, 2913–2920.
26. Wilson, H. L., and Rajagopalan, K. V. (2004) The role of tyrosine 343 in substrate binding and catalysis by human sulfite oxidase. *J. Biol. Chem. 279*, 15105–15113.
27. Ho, S. N., Hunt, H. D., Horton, R. M., Pullen, J. K., and Pease, L. R. (1989) Site-directed mutagenesis by overlap extension using the polymerase chain reaction. *Gene 77*, 51–59.
28. Temple, C. A., Graf, T. N., and Rajagopalan, K. V. (2000) Optimization of expression of human sulfite oxidase and its molybdenum domain. *Arch. Biochem. Biophys. 383*, 281–287.
29. Kipke, C. A., Enemark, J. H., and Sunde, R. A. (1989) Purification of prosthetically intact sulfite oxidase from chicken liver using a modified procedure. *Arch. Biochem. Biophys. 270*, 383–390.
30. Kessler, D. L., and Rajagopalan, K. V. (1974) Hepatic sulfite oxidase. Effect of anions on interaction with cytochrome c. *Biochim. Biophys. Acta 370*, 389–398.
31. Borek, D., Minor, W., and Otwinowski, Z. (2003) Measurement errors and their consequences in protein crystallography. *Acta Crystallogr. D59*, 2031–2038.
32. McCoy, A. J. (2007) Solving structures of protein complexes by molecular replacement with Phaser. *Acta Crystallogr. D63*, 32–41.
33. Emsley, P., and Cowtan, K. (2004) Coot: Model-building tools for molecular graphics. *Acta Crystallogr. 60*, 2126–2132.
34. Word, J. M., Bateman, R. C., Jr., Presley, B. K., Lovell, S. C., and Richardson, D. C. (2000) Exploring steric constraints on protein mutations using MAGE/PROBE. *Protein Sci. 9*, 2251–2259.
35. Murshudov, G. N., Vagin, A. A., and Dodson, E. J. (1997) Refinement of macromolecular structures by the maximum-likelihood method. *Acta Crystallogr. D53*, 240–255.
36. Davis, I. W., Leaver-Fay, A., Chen, V. B., Block, J. N., Kapral, G. J., Wang, X., Murray, L. W., Arendall, W. B., III., Snoeyink, J., Richardson, J. S., and Richardson, D. C. (2007) MolProbity: All-atom contacts and structure validation for proteins and nucleic acids. *Nucleic Acids Res. 35*, W375–W383.
37. Painter, J., and Merritt, E. A. (2006) Optimal description of a protein structure in terms of multiple groups undergoing TLS motion. *Acta Crystallogr. D62*, 439–450.
38. Cramer, S. P., Tench, O., Yocum, M., and George, G. N. (1998) A 13-Element Ge Detector for Fluorescence EXAFS. *Nucl. Instrum. Methods A266*, 586–591.
39. Rehr, J. J., Mustre de Leon, J., Zabinsky, S. I., and Albers, R. C. (1991) Theoretical X-ray absorption fine structure standards. *J. Am. Chem. Soc. 113*, 5135–5140.
40. Mustre de Leon, J., Rehr, J. J., Zabinsky, S. I., and Albers, R. C. (1991) *Ab initio* curved-wave X-ray absorption fine structure. *Phys. Rev. B 44*, 4146–4156.
41. Frisch, M. J., Trucks, G. W., Schlegel, H. B., Scuseria, G. E., Robb, M. A., Cheeseman, J. R., Montgomery, J. A., Jr., Vreven, T., Kudin, K. N., Burant, J. C., Millam, J. M., Iyengar, S. S., Tomasi, J., Barone, V., Mennucci, B., Cossi, M., Scalmani, G., Rega, N., Petersson, G. A., Nakatsuji, H., Hada, M., Ehara, M., Toyota, K., Fukuda, R., Hasegawa, J., Ishida, M., Nakajima, T., Honda, Y., Kitao, O., Nakai, H., Klene, M., Li, X., Knox, J. E., Hratchian, H. P., Cross, J. B., Bakken, V., Adamo, C., Jaramillo, J., Gomperts, R., Stratmann, R. E., Yazyev, O., Austin, A. J., Cammi, R., Pomelli, C., Ochterski, J. W., Ayala, P. Y., Morokuma, K., Voth, G. A., Salvador, P., Dannenberg, J. J., Zakrzewski, V. G., Dapprich, S., Daniels, A. D., Strain, M. C., Farkas, O., Malick, D. K., Rabuck, A. D., Raghavachari, K., Foresman, J. B., Ortiz, J. V., Cui, Q., Baboul, A. G., Clifford, S., Cioslowski, J., Stefanov, B. B., Liu, G., Liashenko, A., Piskorz, P., Komaromi, I., Martin, R. L., Fox, D. J., Keith, T., Al-Laham, M. A., Peng, C. Y., Nanayakkara, A., Challacombe, M., Gill, P. M. W., Johnson, B., Chen, W., Wong, M. W., Gonzalez, C., and Pople, J. A. (2004) Gaussian 03, revision E.01, Gaussian, Inc., Wallingford, CT.
42. Hay, P. J., and Wadt, W. R. (1985) *Ab initio* effective core potentials for molecular calculations. Potentials for the transition metal atoms Sc to Hg. *J. Chem. Phys. 82*, 270–283.
43. Graham, D. C., Christian, G., Stranger, R., and Yates, B. F. (2009) The Influence of Peripheral Ligand Bulk on Nitrogen Activation by 3-Coordinate Molybdenum Complexes: A Theorectical Study using the ONIOM Method. *J. Comput. Chem.,* 2146–2156.
44. Cances, E., Mennucci, B., and Tomasi, J. (1997) A new integral equation formalism for the polarizable continuum model: Theoretical background and applications to isotropic and anisotropic dielectrics. *J. Chem. Phys. 107*, 3032–3041.
45. Mennucci, B., Cances, E., and Tomasi, J. (1997) Evaluation of Solvent Effects in Isotropic and Anisotropic Dielectrics and in Ionic Solutions with a Unified Integral Equation Method: Theoretical Bases, Computational Implementation, and Numerical Applications. *J. Phys. Chem. B 101*, 10506–10517.
46. Mennucci, B., Cammi, R., and Tomasi, J. (1999) Analytical free energy second derivatives with respect to nuclear coordinates: Complete formulation for electrostatic continuum solvation models. *J. Chem. Phys. 110*, 6858–6870.
47. Hilton, J. C., and Rajagopalan, K. V. (1996) Identification of the molybdenum cofactor of dimethyl sulfoxide reductase from *Rhodobacter sphaeroides* f. sp. *denitrificans* as bis(molybdopterin guanine dinucleotide)molybdenum. *Arch. Biochem. Biophys. 325*, 139–143.
48. Matthews, B. W. (1968) Solvent content of protein crystals. *J. Mol. Biol. 33*, 491–497.
49. Cramer, S. P., Gray, H. B., and Rajagopalan, K. V. (1979) The molybdenum site of sulfite oxidase. Structural information from X-ray absorption spectroscopy. *J. Am. Chem. Soc. 101*, 2772–2774.
50. George, G. N., Kipke, C. A., Prince, R. C., Sunde, R. A., Enemark, J. H., and Cramer, S. P. (1989) Structure of the active site of sulfite oxidase. X-ray absorption spectroscopy of the Mo(IV), Mo(V), and Mo(VI) oxidation states. *Biochemistry 28*, 5075–5080.
51. Harris, H. H., George, G. N., and Rajagopalan, K. V. (2006) High-resolution EXAFS of the active site of human sulfite oxidase: Comparison with density functional theory and X-ray crystallographic results. *Inorg. Chem. 45*, 493–495.
52. George, G. N., Pickering, I. J., and Kisker, C. (1999) X-ray Absorption Spectroscopy of Chicken Sulfite Oxidase Crystals. *Inorg. Chem. 38*, 2539–2540.
53. Kutzler, F. W., Natoli, C. R., Misemer, D. K., Doniach, S., and Hodgson, K. O. (1980) Use of one-electron theory for the interpretation of near edge structure in K-shell X-ray absorption spectra of transition metal complexes. *J. Chem. Phys. 73*, 3274–3288.
54. George, G. N., Hilton, J., and Rajagopalan, K. V. (1996) X-ray absorption spectroscopy of dimethyl sulfoxide reductase from *Rhodobacter sphaeroides*. *J. Am. Chem. Soc. 118*, 1113–1117.
55. Partyka, D. V., and Holm, R. H. (2004) Oxygen/sulfur substitution reactions of tetraoxometalates effected by electrophilic carbon and silicon reagents. *Inorg. Chem. 43*, 8609–8616.